

# RESOLUTION TESTS OF GLOBAL GEODYNAMIC MODELS BY TRAVEL-TIME TOMOGRAPHY

Marie Běhounková<sup>1,2</sup>, Hana Čížková<sup>1</sup> and Ctirad Matyska<sup>1</sup>

<sup>1</sup>*Department of Geophysics, Faculty of Mathematics and Physics,  
Charles University, Prague*

<sup>2</sup>*Institute of Geophysics, Czech Academy of Science, Prague*

## ABSTRACT

This study presents results of a 2-D tomographic inversion of synthetic data that examines the ability of seismic tomography to reveal structures created by mantle dynamic processes. Our seismic velocity anomaly model is based on the density heterogeneities obtained from models of thermal and thermo-chemical convection. Both layered and whole-mantle models are employed to produce the synthetic input anomalies. We investigate the resolving power of the inversion of P and PP arrival-times, and assess the influence of parameterisation and regularisation (damping). We show that the effect of regularisation is substantial and that the optimum damping depends upon the wavelength of the input structures. The resolution of the inversion decreases considerably at depths greater than 1000 km, therefore the ability of the kinematic inversion to distinguish between whole-mantle and layered flows (coupled via thermal coupling) may be limited.

## 1. INTRODUCTION

Seismic tomography is one of the most powerful tools yielding information about the internal structure of the Earth and, consequently, its dynamic processes. Geodynamicists and geochemists have been puzzling about the style of mantle circulation for decades (for review see e.g. *Tackley, 2000*). One of the main questions, which is still not resolved, is whether the convection is whole mantle or layered. In the late nineties, the resolving power of seismic tomography has allowed relatively narrow structures to be mapped. These structures are probably connected to subducting slabs (*van der Hilst et al., 1997; Grand et al., 1997; Bijwaard et al., 1998*) or even hotspot plumes (*Montelli et al., 2004*). The question, however, remains how to interpret these results and how to use them to distinguish between different scenarios of mantle circulation.

Since seismically fast slab-like downwelling structures were found to penetrate the 660 km interface and extend into the lower mantle, sometimes even to the core-mantle boundary (CMB) (*van der Hilst et al., 1997; Bijwaard et al., 1998*), the results of seismic tomography are often interpreted as a support for the whole-mantle convection scenario. However, the results of tomographic inversion are not unique. Tomographic images depend upon the data selection, on the employed inversion method and on the parameterisation. Moreover, the tomographic resolution can be very poor in some regions due to the uneven distribution of sources and receivers. Since the effect of all these factors to imaging the mantle structure is not fully clear, it is questionable whether we are able to infer the style of mantle convection from the

---

<sup>1</sup>Address: V Holešovičkách 2, 182 00 Prague 8, Czech Republic  
(fax 221912555, e-mail: behounek@karel.troja.mff.cuni.cz)

<sup>2</sup>Address: Boční II/1401, 141 31 Prague 4, Czech Republic

tomographic inversions. To evaluate the resolving power of tomographic inversion, several resolution tests were introduced. The checker-board test (e.g. *Inoue et al., 1990; Su et al., 1994; Vasco et al., 1995; Káráson and van der Hilst, 2001; Fukao et al., 2003*) or layer-cake test (e.g. *Bijwaard et al., 1998*) are often used to check the lateral or radial smearing of input structures. In these tests, either an artificial synthetic input structure is used, which is not connected to the (expected) mantle structure, or an input is chosen on the basis of the real data tomographic inversion output. However, false conclusions may be derived from such simple experiments, as was clearly demonstrated by *Lévêque et al. (1993)*, who dealt with the spectral analysis of the resolution matrix.

Another problem is, that in these tests, the wavelength of the input velocity anomalies is usually bigger than, or equal to, the used basic cells. It has been shown by *Trampert and Snieder (1996)* that the small scale anomalies that are not contained in the model parameterisation cause leakage into the longer wavelength solution and bias the retrieved model. In other words, the projection error of synthetic structures in standard synthetic resolution tests is much smaller or even negligible in comparison with the projection error of real structure where the wavelength distribution is not limited.

To perform a more correct synthetic resolution test, some physical model of seismic velocity structure is needed that contains the structures of diverse wavelengths. This model should be as close as possible to the (expected) real mantle structure. Such a synthetic input structure can be constructed on the basis of thermal convection models (*Bunge and Davies, 2001*). We perform the synthetic tomographic inversion for four different models of mantle convection (whole-mantle and layered; different viscosity stratification). For all of them, we compare the synthetic input anomalies with the inversion output and try to answer the question as to what is the resolving power of the tomographic inversion in certain parts of the mantle. We are particularly interested in the situation near the impermeable boundary in the layered convection models as we would like to find out whether the inversion is able to distinguish between the seemingly continuous structures generated by thermal coupling mechanism (*Čížková and Matyska, 2004*) and really continuous structures developed in the whole-mantle models.

## 2. METHOD

In the travel-time tomography, the arrival times of body waves are used to determine the wavespeed. Travel-time  $T$  of body wave along a ray path  $L$  (depending upon slowness) is given by

$$T = \int_L s(\mathbf{r}) dl, \quad L = L(s), \quad (1)$$

where  $s$  denotes the slowness and  $\mathbf{r}$  the position vector. The reference travel time,  $T_0$ , of an a priori model of slowness,  $s_0$ , is defined as

$$T_0 = \int_{L_0} s_0(r) dl_0, \quad L_0 = L_0(s_0), \quad (2)$$

where the subscript 0 denotes reference model quantities and the reference slowness,  $s_0$ , is a depth-dependent function. In tomographic inversions, delay,  $d$ , is usually

defined as

$$d = T - T_0 + \epsilon = \int_{L_0} \Delta s dl_0 + \epsilon + \xi, \quad (3)$$

where  $\epsilon$  is the picking error,  $\Delta s$  is the difference between slowness,  $s$ , and reference slowness,  $s_0$ , and  $\xi$  represents the error arising from approximating the path,  $L$ , by the reference path  $L_0$ .

To solve the problem (3), we use the irregular cell parameterisation proposed by *Bijwaard et al. (1998)*:

$$\Delta s(\mathbf{r}) = \sum_{k=1}^M s_k c_k(\mathbf{r}) + \zeta(\mathbf{r}), \quad (4)$$

where  $c_k(\mathbf{r})$ ,  $k = 1, \dots, M$  is an irregular orthogonal basis in  $L_2$  ( $c_k(\mathbf{r})=1$  if  $\mathbf{r}$  is in the  $k^{th}$  cell,  $c_k(\mathbf{r})=0$  elsewhere),  $s_k$  are unknown projection coefficients and  $\zeta(\mathbf{r})$  is a projection error. To construct the irregular base, we adopt the algorithm of *Spakman and Bijwaard (2001)*.

Substituing (4) into (3) and considering  $N$  rays results in the set of linear equations

$$\mathbf{d} = \mathbf{G}\mathbf{m} + \mathbf{e}, \quad (5)$$

where  $d_i$ ,  $i = 1, \dots, N$  represents the delay of  $i^{th}$  ray,  $G_{ij}$  is an arc length of the  $i^{th}$  ray in the  $j^{th}$  cell,  $m_j$  is the  $j^{th}$  model parameter ( $m_j = C_j^{-\frac{1}{2}} s_j$ ,  $C_j$  is the volume of the  $j^{th}$  cell) and  $e_i = \epsilon_i + \xi_i + \bar{\zeta}_i$ , where  $\bar{\zeta}_i$  is integral of projection error  $\zeta(\mathbf{r})$  along the  $i^{th}$  reference ray. In this study, we will not take into account the picking error (i. e.  $\epsilon_i = 0$ ,  $\forall i$ ). We first determine the reference ray,  $L_0$ , by seismic-ray tracing (*Červený et al., 1988*) and then we compute the delay  $d_i$  by integrating the synthetic model slowness along  $L_0$  and neglect the approximation error  $\xi$ . Therefore, the whole unpredictable part of equation (5) will be interpreted as the projection error  $\zeta$ .

We assume an overdetermined inverse problem ( $N > M$ ) and we search for the solution by minimising the misfit functional  $S$ :

$$S = \|\mathbf{G}\mathbf{m} - \mathbf{d}\|_{l_2}^2 + \lambda^2 \|\mathbf{m}\|_{l_2}^2, \quad (6)$$

where the minimalisation of  $\|\mathbf{m}\|_{l_2}$  is equal to the minimalisation of  $\|\sum_k m_k c_k C_k^{-\frac{1}{2}}(\mathbf{r})\|_{L_2}$  due to scaling  $m_j = C_j^{-\frac{1}{2}} s_j$ . We minimise the difference between the observed and predicted data and simultaneously the model vector,  $\mathbf{m}$ , with the weight coefficient (damping factor)  $\lambda$ . In order to solve (6) we use LSQR algorithm by *Paige and Saunders (1982)* and its numerical implementation (<http://www.stanford.edu/group/SOL/software/lqr.html>).

When solving the synthetic problem, we know both the input and output seismic velocity structures. Therefore, we can compare the input synthetic model and inversion result using the correlation coefficient  $\rho$

$$\rho = \frac{\int_V f(\mathbf{r})g(\mathbf{r})dV}{\|f\|_{L_2} \cdot \|g\|_{L_2}}, \quad (7)$$

$$\|f\|_{L_2}^2 = \int_V f(\mathbf{r})f(\mathbf{r})dV.$$

In this study we will perform the inversion on an axially symmetric two-dimensional spherical domain described by means of the radial distance,  $r$ , and colatitude,  $\theta$ , i. e.  $dV = r dr d\theta$ . Since the ray coverage strongly depends on depth, we also calculate the correlation coefficient  $\rho(r)$  as a function of radius,  $r$

$$\rho(r) = \frac{\int_0^{2\pi} f(\mathbf{r})g(\mathbf{r})r d\theta}{\|f\|_{\Omega} \cdot \|g\|_{\Omega}}, \quad (8)$$

$$\|f\|_{\Omega}^2 = \int_0^{2\pi} f(\mathbf{r})f(\mathbf{r})r d\theta.$$

There are a number of factors that limit the resolving power of seismic tomography. One of them is the correspondence between the seismic velocity structure and the parameterisation chosen for the inversion. For example, we cannot resolve structures smaller than the parameterisation cells. Therefore, the projection of the synthetic input structure to the linear span of the parameterisation functions (an average anomaly over each cell in our case) is the best possible result we could obtain under otherwise ideal circumstances. The projection  $\bar{f}_i$ ,  $i = 1, \dots, M$  of the synthetic model on the basis function  $c_i$  is

$$\bar{f}_i = \frac{\int_V f(\mathbf{r})dV}{C_i}. \quad (9)$$

For the projection error  $\zeta$ , we can write

$$\zeta(\mathbf{r}) = f(\mathbf{r}) - \bar{f}(\mathbf{r}), \quad (10)$$

where  $\bar{f}(\mathbf{r}) = \bar{f}_i$ , if  $\mathbf{r}$  is in the  $i^{th}$  cell. As the last characteristic of inversion result, we define the percentage fit,  $p$ , by

$$p = \left(1 - \frac{\|\mathbf{d}^{\text{pred}} - \mathbf{d}\|^2}{\|\mathbf{d}\|^2}\right) \cdot 100\%, \quad (11)$$

where  $\mathbf{d}^{\text{pred}} = \mathbf{G}\mathbf{m}$ .

### 3. CONSTRUCTION OF INPUT SEISMIC VELOCITY ANOMALIES

Synthetic seismic velocity anomalies are derived from models of thermal and thermochemical convection (*Čížková and Matyska, 2004*). We assume that density anomalies linearly depend only on temperature:

$$\Delta\rho(\mathbf{r}) = -\rho_M\alpha\Delta T(\mathbf{r}), \quad (12)$$

where  $\rho_M = 4500 \cdot \text{kg m}^{-3}$  is reference density of the convection model and  $\alpha = 1.4 \cdot 10^{-5} \text{K}^{-1}$  is thermal expansivity. Relative density and seismic velocity anomalies are coupled by the equation

$$\frac{\Delta\rho(\mathbf{r})}{\rho_0(r)} = p_k(r) \frac{\Delta v(\mathbf{r})}{v_0(r)}, \quad (13)$$

where  $\rho_0(r)$  and  $v_0(r)$  are the reference density and velocity (*Dziewonski and Anderson, 1981*) and  $p_k(r)$  is the proportionality factor (*Karato, 1993*).

We use four models of mantle convection that represent four different scenarios. *Model A* employs thermo-chemical convection with a compositional boundary at a depth of 1000 km. This location is compatible with some geochemical data, seismic observations and geodynamic indications (for review see *Anderson, 2002*). Viscosity depends on the average temperature and pressure at each depth. A low-viscosity channel thus develops near the boundary (*Čížková and Matyska, 2004*) and the flow systems in the upper and lower layers are coupled thermally. *Model B* is again a model of thermo-chemical convection with an impermeable boundary at 1000 km depth but with mechanical coupling (viscosity is constant throughout the mantle except for the high-viscosity lithosphere). The upper and lower layer flow systems are thus coupled mechanically. *Model C* is a model of whole-mantle thermal convection (viscosity is constant except for the high-viscosity lithosphere). *Model D* is again a model of thermo-chemical convection with an impermeable boundary at the depth of 1000 km, however, viscosity increases by two orders of magnitude at the interface and therefore long-wavelength anomalies appear below the boundary. Such broader anomalies could be more easily detected by tomographic inversion. Additional characteristic parameters describing models A-D are given in Tab. 1.

#### *Sources and receivers.*

Having defined the input velocity anomalies, we must now choose the synthetic rays to define the inverse problem. The sources and receivers in our 2-D model should simulate the uneven distribution of earthquake foci and seismic stations on the real Earth. To obtain this, we design the sources and receivers using following algorithm. First, we choose the station network and event location (ISC, years 1964-2001,  $m_b > 4.5$ ) Then, we select two points defining the great circle. One point is chosen to be the geodynamic pole (*Pavoni, 1981; Matyska, 1995*). The second point is chosen such that the great circle is more-less perpendicular to the subduction zones (Fig. 1). The geodynamic pole should be connected to the African and Pacific superswells. Since in the axis of our axisymmetric convection model there is usually also an upwelling (plume), this choice of great circle should enable us to be as close to 'reality' as possible in a 2-D simplification. Then we choose the half-width,  $\varphi$ , of a band around a great circle. All sources and receivers within distances smaller than  $\varphi$  from the great circle are projected onto the great circle's plane. In our model,  $\varphi$  is  $8^\circ$ . Then we apply the condition that the minimum distance of sources has to be  $2^\circ \times 2$  km. Closer sources are not taken into account. Similar conditions (a minimum distance of  $0.5^\circ$ ) is applied to the receivers (Fig. 1). This condition is necessary to avoid linearly dependent rows in the matrix  $\mathbf{G}$ . Finally, we choose half of selected points and mirror them around the point defining the great circle that is identical to the geodynamic pole. Velocity anomalies are axisymmetric, hence we need an axisymmetric distribution of sources and receivers. The distributions of sources and receivers used in this study are shown in Fig. 2. We make use of 2366 sources and 184 receivers, which is a realistic ratio used in real tomographic inversions.

We use teleseismic (epicentral distance  $\Delta > 25^\circ$ ) P and pP waves. Ray tracing is performed using the program CRT (<http://sw3d.mff.cuni.cz>; *Červený et al., 1988*). PREM (*Dziewonski and Anderson, 1981*) without an ocean layer is used as the reference model. The total number of rays is 273140.

## 4. RESULTS

### Hit equalising algorithm

Since the distribution of our sources and receivers mimics the real Earth, we also obtain a very irregular ray coverage. This means that if the model were discretised using regular equiangular cells, some of them would be very poorly covered. In Fig. 3a, equiangular cells with a size of  $\Delta\theta = 0.6^\circ$  are shown, while the number of rays passing through them is plotted in Fig. 3c. We note that there are many cells that do not contain any rays, and therefore their slowness is not constrained. On the other hand, other cells are hit by more than 1000 rays, so in some areas a resolution of  $0.6^\circ$  is well justified. Applying the hit equalising algorithm of *Spakman and Bijwaard (2001)* and constructing the irregular parameterisation cells enables us to maintain a high resolution in the well-covered areas, and still have all cells constrained by approximately the same number of rays. The irregular parameterisation obtained as a result of the hit-equalising algorithm with the condition of a minimum of 500 rays per cell is shown in Fig. 3b, and Fig. 3d shows the number of rays in each cell for this parameterisation. By comparing Figs. 3c and 3d it is clear that the ray coverage is now more evenly distributed over the model, although there are still some cells with a very high hit count (up to 1000) due to the high concentration of sources in some regions.

### Projection error

The value of the projection error,  $\zeta$ , is particularly important when solving the inverse problem. The projection error is high, if we are not able to describe the input model by the chosen irregular parameterisation in some area. Some artifacts can then appear in the inversion output near the region with a high projection error. An example of projection error is given in Plate A. In Plate Aa one input seismic velocity model (based on convection model A) is shown. Its projection to the basis function (Fig. 3b) is given in Plate Ab. Clearly the fine input structure cannot be reproduced well by means of the large parameterisation cells in some areas (e.g. the area close to the symmetry axis on the left hand side). In these regions, the projection (approximation) error (Plate Ac) is large.

### Influence of parameterisation

It is clear that the results from the inversion depends upon the chosen parameterisation. Therefore, it is very important to test various parameterisation. In Fig. 4, three different parameterisations are shown. Parameterisations P500 and P1000 have the same basis function. The model is divided into 24000 equiangular cells ( $\Delta\theta = 0.6^\circ$ , thickness of each cell  $\sim 72$  km), after which the hit equalising algorithm is applied. We require a minimum of 500 rays in each cell for parameterisation P500, and 1000 rays for parameterisation P1000. The third parameterisation model, P500+1000, is divided into 24000 equiangular cells ( $\Delta\theta = 0.6^\circ$ , thickness of each cell  $\sim 50$  km above boundary at the depth 1000 km and  $\sim 95$  km below the boundary). We require a minimum of 500 rays in each cell above the boundary and 1000 rays below the boundary. The number of cells in each parameterisation is given in Tab. 2. The form of each parameterisation after the application of the hit-equalising algorithm and their associated hit count are shown in Fig. 4. The results of the inversion for damping coefficient  $\lambda = 1000$  are illustrated in Plate B, where one detail of an input structure and inversion output is shown. The highest correlation (the smallest projection error) between the input and the projection on the basis

function is obtained for the parameterisation P500 (Tab. 2). The highest correlation between the input and the output is also reached for the parameterisation P500. The resolution of the inversion is very good in the upper 1000 km of the mantle (Plate B), although it is considerably worse below the boundary. For the parameterisations P500 and P1000, we are not able to resolve either the vertical part of the slow velocity anomaly (plume), nor the cold downwelling initiated below the 1000 km interface. Using the parameterisation P500+1000, the plume basis as well as the slab-like structure are partially detected, although the correlation coefficient is less than the correlation for P500 and P1000 (Tab. 2).

#### Influence of the damping factor

The tomographic inversion is an unstable problem, hence an explicit regularisation is necessary to solve the inversion. We use regularisation in the form (6) to stabilise the inverse problem, a consequence of which is that the result is sensitive to the damping factor  $\lambda$ . To illustrate the influence of the damping factor, we solve the synthetic inversion for the same input seismic velocity model as in the previous paragraph (Plate Aa using the parameterisation P500). The damping parameter values  $\lambda = 0, 10, 100, 200, 500, 700, 1000$  and  $10000$  are tested. The results are plotted in Plates C and D. The values of the correlation and the percentage fit are listed in Tab. 3. The oscillatory output structure is obtained if no regularisation is applied ( $\lambda = 0$ , Plate Cb). The oscillations are vertical features (amplitude is changing fast in the horizontal direction) in the well ray-covered regions. In poor-coverage regions, oscillations are both horizontal and vertical. The oscillations disappear when the damping factor increases ( $\lambda = 100$ , Plate Cc). However, the regularisation causes the blurring of input anomalies along the rays (e.g. the seismically slow anomaly in the right part of the lower layer - Plate Cc). For the damping factor  $\lambda = 10000$  (Plate Cd), the percentage fit strongly decreases (Tab. 3). In this case the minimisation of the model vector  $\mathbf{m}$  is already much more important than the minimisation of the difference between the observed and predicted data (eq. (6)). A detailed view of one particular structure and its tomographic image for three different values of  $\lambda$  are given in Plate D. For damping factor  $\lambda = 100$  (Plate Db), the solution shows small oscillations, but the two isolated downwellings can be distinguished. They start to blur along the rays with an increase of damping factor ( $\lambda = 200$ , Plate Dc). For damping factor  $\lambda = 500$  (Plate Dd), they already merge to form one structure. Therefore, we suggest an "optimum" value of the damping factor for the chosen parameterisation to lie in the interval between  $\lambda = 100$  and  $\lambda = 500$ . For these values of  $\lambda$ , oscillations of the inversion result are suppressed in well-covered regions. However, artifacts can still appear in the poorly covered regions.

#### Results of the inversion for various models

We used four input seismic-velocity distributions based on the four different convection models. We chose the parameterisation P500 and damping factors  $\lambda = 500$  (models A, B, C) and  $\lambda = 200$  (model D). Percentage fit and correlation values are in Tab. 4. Correlations between input anomalies and their projections onto the basis functions are highest for the models with relatively long-wavelength anomalies (models A and D) and smaller for the models with relatively narrow anomalies (models B and C). The results are summarised in Plate E. For each model, we show details of two different structures. In the first and third columns, the input synthetic anomalies are shown, while the second and fourth column give the inversion outputs.

Model A. In the well-covered regions (Plate *Ea,b*) both seismically fast and slow anomalies are very well resolved in the upper 1000 km of the mantle. Below 1000 km however, the resolution strongly decreases and the correlation between the synthetic input and inversion output drops dramatically (Fig. 5a), where the smearing of both fast and slow anomalies along the rays is clearly visible. The capacity of the inversion in the poorly-covered regions are demonstrated in Plate *Ec,d*, where since the input model cannot be described by the used parameterisation, the result is very poor.

Model B (Plates *Ee-h*) contains narrow, mostly vertical anomalies below the boundary at a depth of 1000 km, so on the basis of the results obtained for the model A, we are not surprised by poor resolution of these features. The upper mantle anomalies are resolved quite well. Beneath the interface the horizontally lying head of the plume (Plate *Ee,f*) in the uppermost part of the lower layer is clearly visible. Also, the uppermost part of a seismically-fast structure originating just below the interface (Plate *Eg,h*) can be traced in the tomographic image. However, no deeper structures are resolved and correlation is very low (Fig. 5b). The seismically-fast anomalies in the lower layer associated with their seismically-slow upper layer counterparts (and vice versa) are, however, clearly visible, so if there were a compositional layering with a mechanical coupling taking place, our inversion would be able to resolve it.

Model C is an example of whole mantle convection. Similarly to the previous model B, it also contains mostly narrow vertical structures. Since no layering occurs, there are basically no strong horizontal anomalies. This is the reason why the inversion is even worse than for the case of model B. In the upper mantle, the seismically-fast structure is well resolved (Plate *Ei,j*) as well as the head of the plume (Plate *Ek,l*). In the lower layer, however, only a few features of the input model are revealed. There is some sign of the small plume head (Plate *Ei,j*) and also weak horizontal anomalies in the right part of Plate *Ek,l*. The smearing of the seismically-fast anomaly (Plate *Ei,j*) along the rays is again observed. Correlation (Fig. 5c) is relatively high above 700 km, but it rapidly decreases below this depth. This is different from the previous (layered) models where the correlation begins to strongly decrease from a greater depth (about 1000 km). That probably occurs because the input structures are narrow throughout the whole mantle and the resolving capability of the tomographic imaging has decreased already by about 700 km. In the layered models the horizontal extent of anomalies increases in the depth interval 700 km - 1000 km. Therefore, they are more easily visible for the tomographic imaging and the quality of the inversion as measured by the correlation coefficient is much better between 700 km and 1000 km depths.

Since the ability of our inversion to detect narrow vertical anomalies is limited, in the last test we concentrate on the model containing only long-wavelength features in the lower layer. The results for model D (layered model with a high viscosity lower layer) are given in Plates *Em-p*. As expected, the results of the inversion are much better in this case and both in the upper and lower layers the basic features of the input structure are revealed. However, the smearing effect is clearly visible even here and although the position of seismically-fast and slow anomalies are detected, their amplitudes are underestimated, especially at a depth of about 2000 km. The correlation between the input and output is relatively high throughout the whole mantle in this case, except around a depth of about 700 km.

### Standard synthetic tests

Finally, we show some results of standard synthetic resolution tests.

*Checker-board test.* The input synthetic structures are boxes including  $4 \times 4$  (model S4 – Fig. 6a) and  $10 \times 10$  (model S10 – Fig. 6e) basic  $0.6^\circ$  cells. The projection of these synthetic structures onto the irregular parameterisation cells P500 are given in Figs. 6b and 6f for models S4 and S10, respectively, and the results for two values of the damping factor  $\lambda$  in Figs. 6c,d and 6g,h, respectively. The results of the inversion for these two different scale input anomalies and several values of  $\lambda$  are summarised in Tab. 5, where the correlation coefficients and amount of percentage fit are given. For low values of the damping factor, the inversion is more successful in resolving the larger-scale anomalies in S10, while for  $\lambda$  between 100 and 1000, the correlation between the input and output is slightly higher for small-scale anomalies in S4. For a very high damping factor, the large-scale anomalies are again better resolved (though the correlation coefficient for both models S4 and S10 is already low here). Hence the influence of the damping coefficient to the results depends upon the wavelength of the input anomalies.

In order to check the effect of  $\lambda$  on the different wavelength anomalies, we performed the checker-board test for five models - the size of the checker-board anomalies being  $1 \times 1$ ,  $8 \times 8$ ,  $20 \times 20$  and the above mentioned  $4 \times 4$  and  $10 \times 10$  basic cells. For all of them we solved the inverse problem with different values of  $\lambda$ , ranging from 10 to 1000 and calculated the correlation between the input and output patterns. In order to eliminate the effect of the poor ray coverage in the left-hand side polar area, we calculated the correlation only over the well covered right-hand side half of our model (see Fig. 6b). The resulting correlation for  $\lambda$  ranging from 10 to 250 is given in Fig. 7a. It is clear that the maximum correlation is found for different size anomalies obtained for different values of  $\lambda$ . The value of  $\lambda$  that gives the maximum correlation is for input models with anomalies of different wavelengths plotted in Fig. 7b. The optimum  $\lambda$  decreases with increasing size of the anomalies, from 200 for the smallest anomalies ( $0.6^\circ$ ) to 20 for the large anomalies ( $12^\circ$ ). The maximum correlation obtained for these optimum combinations of the anomaly size and its preferred  $\lambda$  does not change much (0.905 - 0.940) - see Fig. 7c. Similar tests of the effect of damping on the inversion results for different size anomalies could provide tomographers with a tool that allows the selection of the wavelength-dependent damping, and thus optimise the results of the real data inversion.

*Layer-cake test.* The chosen input anomalies for this test are artificial seismically fast structures (1.5 %) reminding slabs of different widths ( $1.5^\circ$  - Fig. 8a or  $6^\circ$  - Fig. 8e at the surface) dipping into the mantle with an angle of  $30^\circ$ . They are not continuous, hence we can exclude the artificial continuity of each slab due to smearing along rays (*Bijwaard, 1999*). Inversion results are plotted in Fig. 8c,d and 8g,h, and percentage fit and correlation coefficients are given in Tab. 6. The correlation between input and output for anomaly wide  $6^\circ$  is higher than for anomaly wide  $1.5^\circ$ . For the lower damping factor value ( $\lambda = 100$ ) the input structures are better resolved, but the output is biased by small-scale oscillations. For the higher value of  $\lambda$ , these oscillations are suppressed, but the resolving power of the inversion is lower. The narrow structure in the lower mantle is underestimated both in size and amplitude. In the uppermost mantle, certain smearing effects are observed -

the originally isolated 'blobs' are connected (although the amplitude of this 'ghost' connection is lower than the amplitude of the 'real' anomaly). Similar effects can be observed for the wider input anomaly, but they are not so strong.

## 5. CONCLUSIONS

Although we have limited ourselves in this study to two dimensional models, it gives some information that is not provided by standard resolution tests that usually ignore the projection error. We show here that the effects of parameterisation and regularisation are very strong, especially the damping has very strong influence on the inversion output. By 'tuning' the damping factor, we are able to obtain quite successful output. However, in a real data inversion, we have no direct tool for yielding an optimum regularisation. The fact, that the 'ideal' value of damping coefficient depends upon the size of seismic velocity anomalies makes the problem even more complicated.

In our convection models, a compositional interface causing layered convection is prescribed at a depth of 1000 km. We are particularly interested in the structures of the convection currents in the lower layer, especially the question of whether the tomographic inversion is able to distinguish between the continuous downwellings (whole mantle models) and thermally coupled structures (layered models). This is important as it allows us to judge the ability of tomography to provide evidence (or at least strong preference) for one or another concept of mantle circulation. In our inversion setup, the resolution decreases considerably at a depth of about 1000 km and the deeper vertical structures remain often unresolved. The question then arises as to the geodynamical implication often drawn on the basis of the real data kinematic inversions performed using a similar methodology. It is clear that our results are inevitably negatively influenced by the adopted two-dimensional simplification of the model. Nevertheless, we believe that our study points to the requirement of more detailed resolution tests in tomographic inversions of real data.

### **Acknowledgements**

We thank Luděk Klimeš for providing his code for ray tracing and for valuable advices, Ondřej Čadek, Arie van den Berg and Jeroen van Hunen for inspiring discussions and Kevin Fleming for English correction. This work was supported by the research projects GAUK 376/2004, GACR 205/02/1306 and DG MSM 113200004.

- Anderson, D., 2002: The Case of Irreversible Chemical Stratification. *International Geology Review*, **44**, 97-166.
- Bijwaard, H., 1999: Seismic Travel-Time Tomography for Detailed Global Mantle Structure. Phd thesis, Utrecht University.
- Bijwaard, H., Spakman, W. and Engdahl, E. R., 1998: Closing the Gap between Regional and Global Travel Time Tomography. *Journal of Geophysical Research*, **103**, 30055-30078.
- Bunge, H. P., Davies, J. H., 2001: Tomographic Images of a Mantle Circulation Model. *Geophysical Research Letters*, **28**, 77-80.
- Čížková, H., Matyska, C., 2004: Layered Convection with an Interface at a Depth of 1000 km: Stability and Generation of Slab-like Downwellings. *Physics of the Earth and Planetary Interiors*, **141**, 269-279.
- Červený, V., Klimeš, L., Pšenčík, I., 1988: Complete Seismic-Ray Tracing in Three-Dimensional Structures. In: Doornbos, D.J. (ed.), *Seismological Algorithms*, pp. 89-168, Academic Press, New York.
- Dziewonski, A. M., Anderson, D. L., 1981: Preliminary Reference Earth Model. *Physics of the Earth and Planetary Interiors*, **25**, 297-356.
- Fukao, Y., To, A., Obayashi, M., 2003: Whole Mantle Tomography Using P and PP-P Data. *Journal of Geophysical Research*, **108**.
- Grand, S. P., van der Hilst, R. D., Widiyantoro, S., 1997: Global seismic tomography: A snapshot of convection in the Earth. *GSA Today*, **7**, 1-7.
- Inoue, H., Fukao, Y., Tanabe, K. and Ogata, Y., 1990: Whole mantle P-wave travel time tomography. *Physics of the Earth and Planetary Interiors*, **59**, 294-328.
- ISC International Seismological Centre, On-li Bulletin, <http://www.isc.ac.uk/Bull>, International Seismological Centre, Thatcham, United Kingdom.
- Kárason, H., van der Hilst, R. D., 2001: Tomographic Imaging of the Lowermost Mantle with Differential Times of Refracted and Diffracted Core Phases (PKP,  $P_{diff}$ ). *Journal of Geophysical Research*, **106**, 6569-6587.
- Karato, S., 1993: Importance of Anelasticity in the Interpretation of Seismic Tomography. *Geophysical Research Letters*, **20**, 1623-1626.
- Lévéque, J.-J., Rivera, L., Wittlinger, G., 1993: On the Use of the Checkerboard Test to Assess the Resolution of Tomographic Inversion. *Geophysical Journal International*, **115**, 313-318.
- Matyska, C., 1995: Axisymmetry of Mantle Aspherical Structures. *Geophysical Research Letters*, **22**, 521-524.
- Montelli, R., Nolet, G., Dahlen, F. A., Masters, G., Engdahl, E. R., Hung, S.-H., 2004: Finite-Frequency Tomography Reveals a Variety of Plumes in the Mantle. *Science*, **203**, 338-343.
- Paige, C. C., Saunders, M. A., 1982: LSQR: An Algorithm for Sparse Linear Equations and Sparse Least Squares. *ACM Transaction on Mathematical Software*, **8**, 43-71.
- Pavoni, N., 1981: A Global Geotectonic Reference System Inferred from Cenozoic Tectonics. *Geologische Rundschau*, **70**, 189-206.
- Spakman, W., Bijwaard, H., 2001: Optimization of Cell Parameterization for Tomographic Inverse Problems. *Pure and Applied Geophysics*, **158**, 1401-1423.
- Su, W.-J., Woodward, R. L., Dziewonski, A. M., 1994: Degree-12 Model of Shear

- Velocity Heterogeneity in the Mantle. *Journal of Geophysical Research*, **99**, 6945-6980.
- Tackley, P., 2000: Mantle Convection and Plate Tectonics: Toward and Integrated Physical and Chemical Theory. *Science*, **228**, 2002-2007.
- Trampert, J., Snieder, R., 1996: Model Estimations Biased by Truncated Expansions: Possible Artifacts in Seismic Tomography. *Science*, **271**, 1257-1260.
- van der Hilst, R. D., Widiyantoro, S., Engdahl, E. R., 1997: Evidence for Deep Mantle Circulation from Global Tomography. *Nature*, **386**, 578-584.
- Vasco, D. W., Johnson L. R., Pulliam, R. J., 1995: Lateral Variation in Mantle Velocity Structure and Discontinuities Determined from P, PP, S, SS and SS-SdS Travel Time Residuals. *Journal of Geophysical Research*, **100**, 24037-24059.
- <http://sw3d.mff.cuni.cz>
- <http://www.stanford.edu/group/SOL/software/lqr.html>

$d$	depth of mantle	$2.9 \cdot 10^6$ m
$g$	gravity acceleration	$9.8 \cdot \text{ms}^{-2}$
$\alpha$	thermal expansivity	$1.4 \cdot 10^{-5} \text{K}^{-1}$
$\beta$	compositional contrast	0.03
$R$	internal heating	$3 \cdot 10^{-8} \text{W m}^{-3}$
$\kappa$	thermal diffusivity	$2.5 \cdot 10^{-6} \text{m}^2\text{s}^{-1}$
$\rho_M$	density of mantle	$4.5 \cdot 10^3 \text{kg m}^{-3}$
$\eta$	viscosity	
$Ra$	Rayleigh's number	$\frac{\rho_M g \alpha \Delta T d^3}{\kappa \eta}$

**Table 1:** Additional characteristics of use convection models

	P500	P1000	P500+1000
number of cells	18108	13005	11627
$p$ [%]	99.72	99.64	99.58
$\rho_{\text{input} \times \text{output}}$	0.789	0.731	0.725
$\rho_{\text{input} \times \text{projection}}$	0.951	0.931	0.939
$\rho_{\text{projection} \times \text{output}}$	0.830	0.785	0.772

**Table 2:** Influence of parameterisation, correlation  $\rho$  and percentage fit  $p$ .

$\rho_{\text{input} \times \text{projection}} = 0.951$								
$\lambda$	0.	10.	100.	200.	500.	700.	1000.	10000.
$p$ [%]	99.85	99.85	99.85	99.84	99.81	99.78	99.72	80.36
$\rho_{\text{input} \times \text{output}}$	0.271	0.381	0.663	0.721	0.777	0.788	0.789	0.624
$\rho_{\text{projection} \times \text{output}}$	0.285	0.401	0.698	0.758	0.818	0.828	0.830	0.657

**Table 3:** Influence of damping to the inversion, percentage fit  $p$  and correlation  $\rho$  for  $\lambda = 0, 10, 100, 200, 500, 700, 1000$  a  $10000$ .

model	A	B	C	D
$\lambda$	500	500	500	200
$p$ [%]	99.94	99.90	99.50	99.96
$\rho_{\text{input} \times \text{output}}$	0.804	0.658	0.649	0.780
$\rho_{\text{input} \times \text{projection}}$	0.947	0.878	0.877	0.973
$\rho_{\text{projection} \times \text{output}}$	0.849	0.750	0.738	0.801

**Table 4:** Percentage fit  $p$  and correlation  $\rho$  for various model.

input velocity anomalies S4					
$\rho_{\text{input} \times \text{projection}} = 0.932$					
	$\lambda = 0$	$\lambda = 10$	$\lambda = 100$	$\lambda = 1000$	$\lambda = 10000$
$p$ [%]	99.97	99.97	99.95	98.96	53.66
$\rho_{\text{input} \times \text{output}}$	0.364	0.482	0.776	0.693	0.426
$\rho_{\text{projection} \times \text{output}}$	0.390	0.517	0.832	0.743	0.457
input velocity anomalies S10					
$\rho_{\text{input} \times \text{projection}} = 0.951$					
	$\lambda = 0$	$\lambda = 10$	$\lambda = 100$	$\lambda = 1000$	$\lambda = 10000$
$p$ [%]	99.99	99.99	99.99	99.67	68.21
$\rho_{\text{input} \times \text{output}}$	0.511	0.621	0.752	0.671	0.481
$\rho_{\text{projection} \times \text{output}}$	0.538	0.654	0.791	0.706	0.507

**Table 5:** Percentage fit  $p$  and correlation  $\rho$  for checker-board test.

input anomalies	$L_{1.5}$		$L_6$	
$\rho_{\text{input} \times \text{projection}}$	0.904		0.953	
$\lambda$	100	1000	100	1000
$p$ [%]	99.36	98.87	99.81	99.65
$\rho_{\text{input} \times \text{output}}$	0.611	0.773	0.745	0.873
$\rho_{\text{projection} \times \text{output}}$	0.667	0.856	0.781	0.916

**Table 6:** Percentage fit  $p$  and correlation  $\rho$  for layer-cake test.

**Figure 1:** Chosen *a)* event and *b)* station location distribution (circles) used in this study and their projection (crosses) onto the great circle, dashed lines denote subduction zones, two points defining the great circle (solid line) are given by solid squares.

**Figure 2:** Schematic figure of event (crosses) and receiver (triangles) distribution used in this study.

**Figure 3:** Hit count equalising algorithm, *a)* equi-angular cells for  $\Delta\theta = 0.6^\circ$  and *c)* corresponding hit count; *b)* irregular cells derived by hit count equalising algorithm and *d)* corresponding hit count.

**Figure 4:** Various parameterisation, *a), b)* and *c)* cells of irregular parameterisation; *d), e)* and *f)* hit count plots in irregular cells.

**Figure 5:** Correlation for input velocity anomalies and inversion output as a function of depth.

**Figure 6:** Result of checker-board test, *a)* input pattern with  $4 \times 4$  basic cell (model S4), *b)* projection of input pattern *a* on the irregular basis function, *c)* and *d)* inversion output of pattern *a* for damping factor  $\lambda = 100$  and  $\lambda = 1000$ ; *e)* input pattern with  $10 \times 10$  basic cell (model S10), *f)* projection of input pattern *e* on the irregular basis function, *g)* and *h)* inversion output of pattern *e* for damping factor  $\lambda = 100$  and  $\lambda = 1000$ .

**Figure 7:** Correlation for checker-board test, *a)* dependence of correlation on damping coefficient  $\lambda$  for good covered region, *b)* dependence of 'ideal' damping on wavelength of input anomalies (good covered region), *c)* dependence of correlation on wavelength of input anomalies for 'ideal damping' (good covered region).

**Figure 8:** Layer-cake test – detail, *a)* input pattern  $L_{1.5}$  – width of anomaly  $1.5^\circ$  on the surface, slope of anomaly  $30^\circ$ , *b)* projection of input pattern *a* on the irregular basis function, *c)* and *d)* inversion output of pattern *a* for damping factor  $\lambda = 100$  and  $\lambda = 1000$ ; *e)* input pattern  $L_6$  – width of anomaly  $6^\circ$  on the surface, slope of anomaly  $30^\circ$ , *f)* projection of input pattern *e* on the irregular basis function, *g)* and *h)* inversion output of pattern *e* for damping factor  $\lambda = 100$  and  $\lambda = 1000$ .

**Plate A:** Projection error, *a)* input seismic velocity anomalies, *b)* projection of input pattern *a* on the irregular basis function, *c)* projection error – equation (10).

**Plate B:** Various parameterisation – detail for  $\theta_A = 55^\circ$  and  $\theta_B = 75^\circ$  ( $\theta_A$  and  $\theta_B$  denote the angles that define the boundaries of the detail plot, see Fig. 2 for definition of  $\theta$ ), *a)* input seismic velocity anomalies; inversion output for parameterisation *b)* P500, *c)* P1000 and *d)* P500+1000 for damping factor  $\lambda = 1000$ .

**Plate C:** Influence of the damping factor, *a)* input seismic velocity anomalies; *b), c)* and *d)* inversion output for damping factor  $\lambda = 0$ ,  $\lambda = 100$  and  $\lambda = 10000$ .

**Plate D:** Influence of the damping factor – detail for  $\theta_A = 95^\circ$  and  $\theta_B = 115^\circ$ , *a)* input seismic velocity anomalies; *b), c)* and *d)* inversion output for damping factor  $\lambda = 100$ ,  $\lambda = 200$  and  $\lambda = 500$ .

**Plate E:** Inversion input and output for various models for a damping factor  $\lambda = 500$  (model A, B and C) and  $\lambda = 200$  (model D). For each model (A – D), the details of two structures are shown.

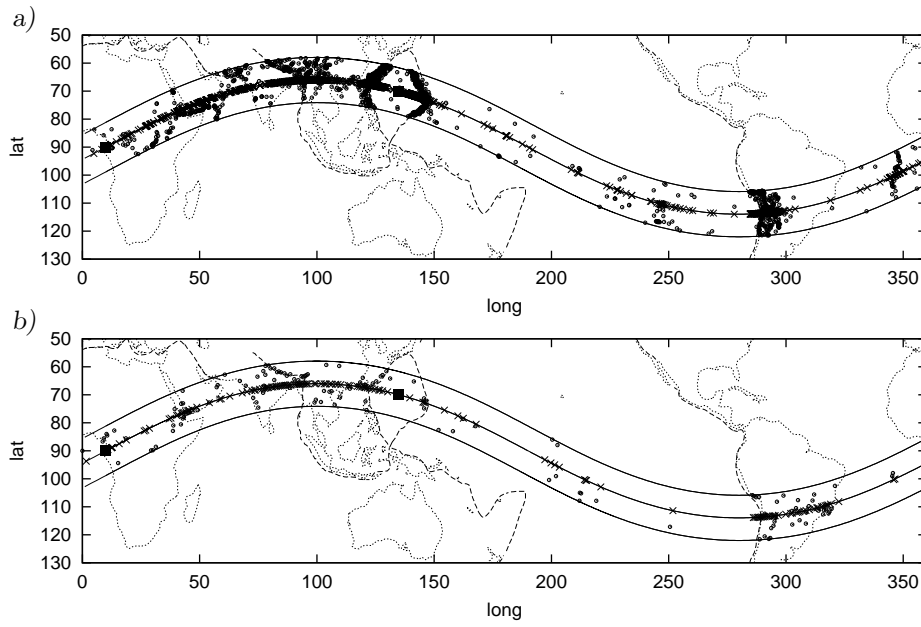


Figure 1:

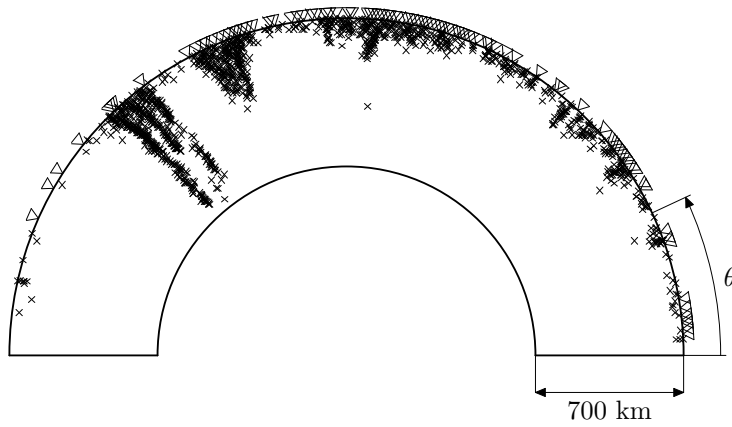


Figure 2:

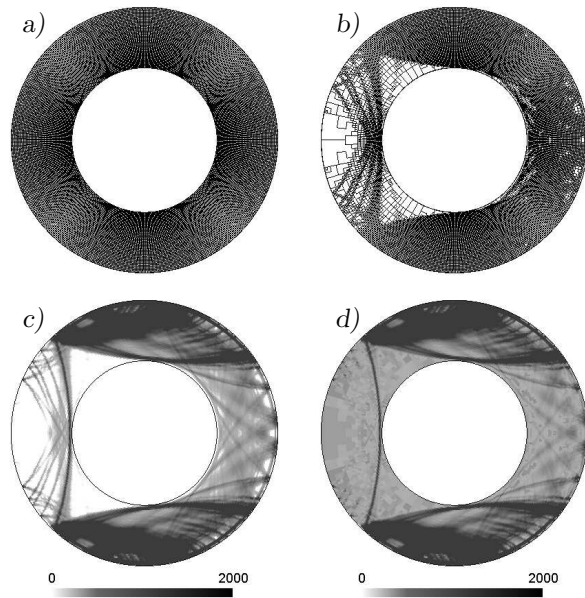


Figure 3:

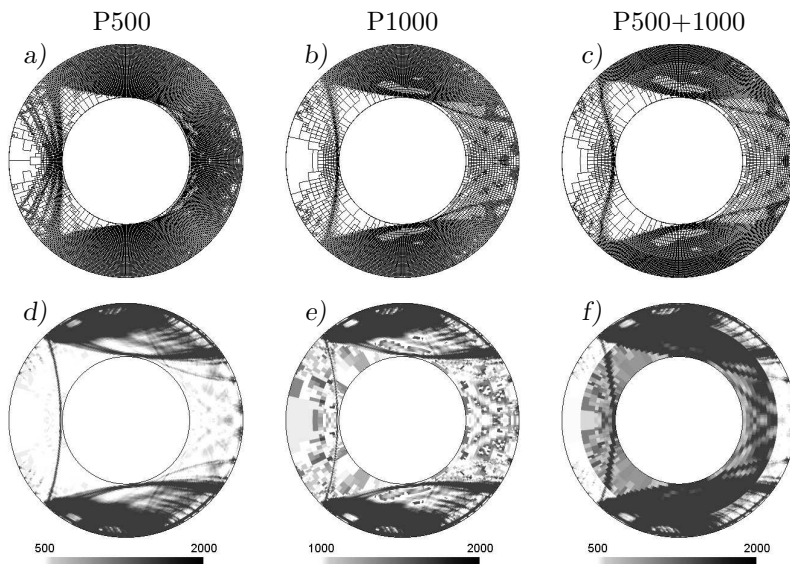


Figure 4:

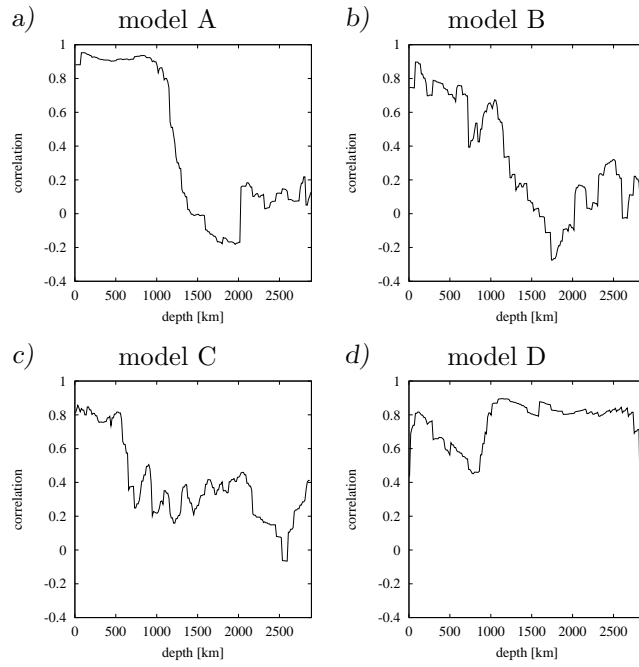


Figure 5:

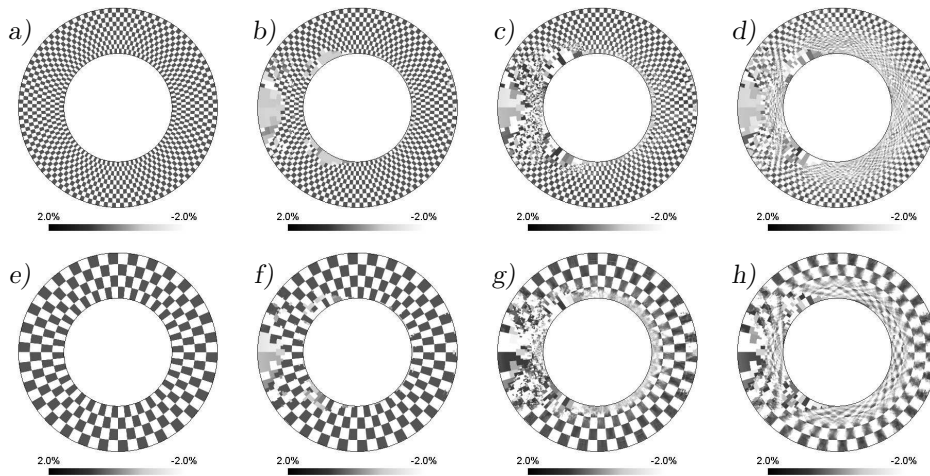


Figure 6:

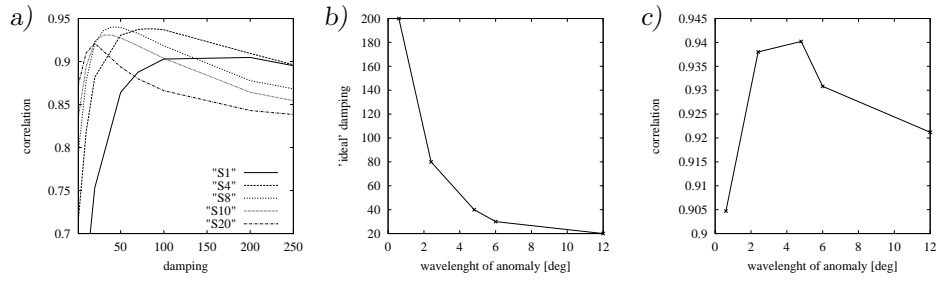


Figure 7:

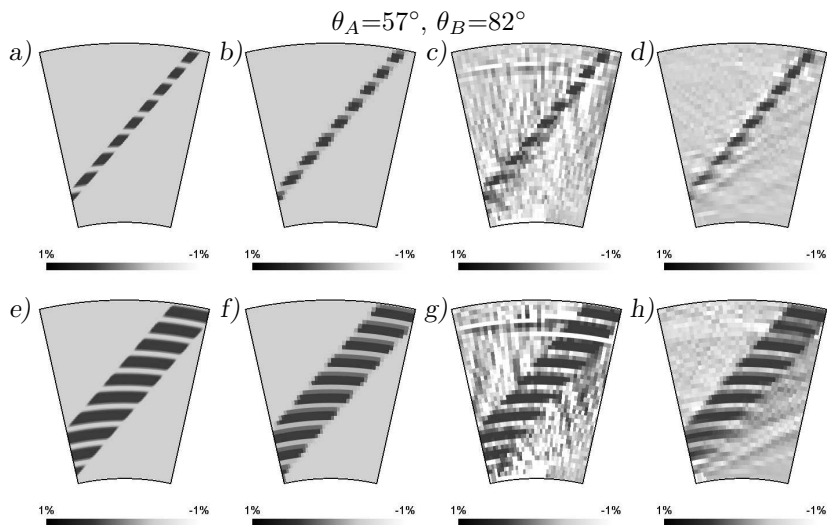


Figure 8:

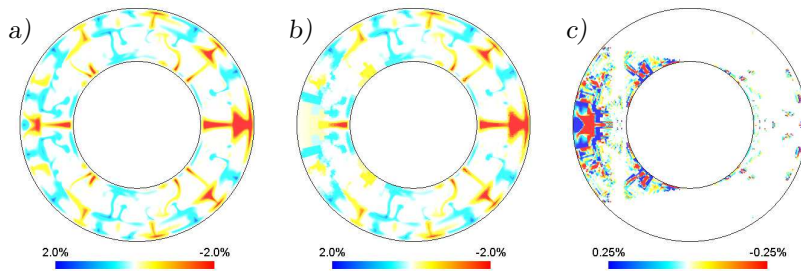


Plate A:

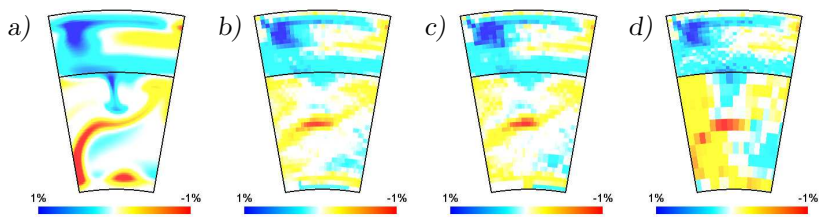


Plate B:

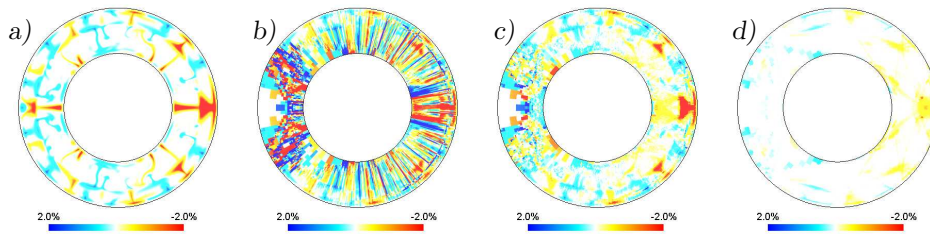


Plate C:

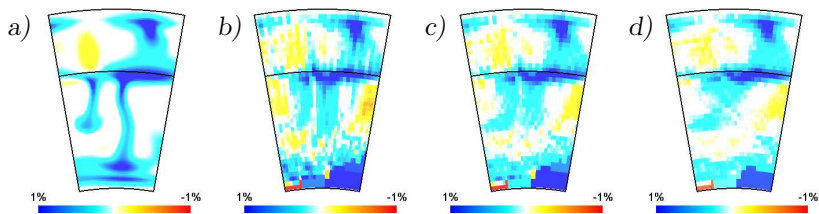


Plate D:

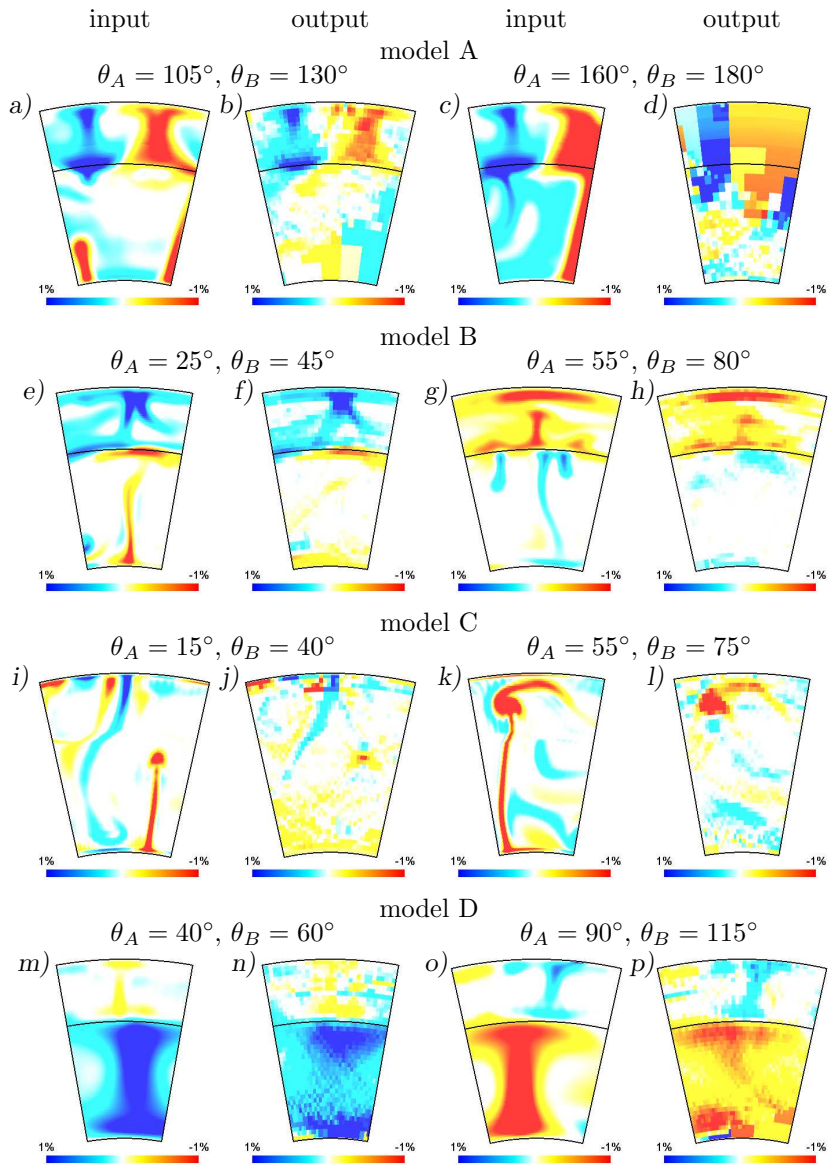


Plate E: